Colloids and Surfaces B: Biointerfaces 216 (2022) 112531

Contents lists available at ScienceDirect

Colloids and Surfaces B: Biointerfaces

journal homepage: www.elsevier.com/locate/colsurfb

Antioxidant colloids via heteroaggregation of cerium oxide nanoparticles and latex beads

Nizar B. Alsharif [a], Gergely F. Samu [b], Szilárd Sáringer [a,b], Adél Szerlauth [a], Dóra Takács [a], Viktoria Hornok [b], Imre Dékány [b], Istvan Szilagyi [a,b,*]

[a] MTA-SZTE Lendület Biocolloids Research Group, University of Szeged, H-6720 Szeged, Hungary
[b] Department of Physical Chemistry and Materials Science, University of Szeged, H-6720 Szeged, Hungary

ARTICLE INFO

Keywords:
Antioxidant
Nanozyme
Composite
Polyelectrolyte
Artificial enzyme

ABSTRACT

Antioxidant colloids were developed via controlled heteroaggregation of cerium oxide nanoparticles (CeO_2 NPs) and sulfate-functionalized polystyrene latex (SL) beads. Positively charged CeO_2 NPs were directly immobilized onto SL particles of opposite surface charge via electrostatic attraction (SL/Ce composite), while negatively charged CeO_2 NPs were initially functionalized with poly(diallyldimethylammonium chloride) (PDADMAC) polyelectrolyte and then, aggregated with the SL particles (SPCe composite). The PDADMAC served to induce a charge reversal on CeO_2 NPs, while the SL support prevented nanoparticle aggregation under conditions, where the dispersions of bare CeO_2 NPs were unstable. Both SL/Ce and SPCe showed enhanced radical scavenging activity compared to bare CeO_2 NPs and were found to mimic peroxidase enzymes. The results demonstrate that SL beads are suitable supports to formulate CeO_2 particles and to achieve remarkable dispersion storage stability. The PDADMAC functionalization and immobilization of CeO_2 NPs neither compromised the peroxidase-like activity nor the radical scavenging potential. The obtained SL/Ce and SPCe artificial enzymes are foreseen to be excellent antioxidant agents in various applications in the biomedical, food, and cosmetic industries.

1. Introduction

Natural enzymes are known to be remarkable biocatalysts that play vital roles in living organisms, they possess exceptional selectivity including enantioselectivity due to their complex chemical structures [1]. In addition to catalyzing metabolic reactions essential to cellular function such as transduction of signals [2] and digestion [3], natural enzymes are widely used in industrial applications as well [4]. For example, enzymes find applications in pharmaceuticals, biofuels, food processing, pulp and paper industry, therapeutic agents, and detergents [4–8]. Despite their flawless catalytic performance, natural enzymes possess several inherent drawbacks such as high sensitivity to operational conditions including the pH and temperature [9]. When subject to undesignated conditions, the vital structures of the comprising proteins gradually denature leading to permanent loss of enzymatic activity, which has rendered their production and purification processes considerably complicated, expensive, and time-consuming [1,9,10]. These drawbacks have prompted the need for alternative materials that have more versatile structures yet possess equally efficient catalytic potential. The reports on fullerene derivatives as superoxide dismutase (SOD) mimics are one of the earliest studies on artificial enzymes [11], and ever since, significant work on artificial enzymes of diverse structures has been reported, including nanomaterials, metal complexes, and polymeric materials [12,13].

Particularly, artificial enzymes based on nanomaterials (nanozymes) are expected to be the optimal alternatives to native enzymes [12–18]. They have low-cost and simple production processes and have structural and functional stability in wide pH and temperature ranges, typically outside the operational range of the mimicked enzymes [19,20]. Most importantly, nanostructured materials have highly tunable physicochemical properties, and can be utilized under numerous industrial conditions, where the native enzymes are non-functional [9,21]. Therefore, nanozymes have been prepared in numerous compositions including metal oxides[22], and chalcogenides [23], carbon derivatives [24], metal-organic frameworks [25], and metallic nanoparticles [26].

Nanoceria or cerium oxide (CeO_2) nanoparticles are non-stoichiometric crystals employed in industrial and biomedical processes alike [27]. For instance, nanoceria has been widely used in numerous

* Corresponding author at: MTA-SZTE Lendület Biocolloids Research Group, University of Szeged, H-6720 Szeged, Hungary.
E-mail address: szistvan@chem.u-szeged.hu (I. Szilagyi).

https://doi.org/10.1016/j.colsurfb.2022.112531
Received 22 March 2022; Received in revised form 25 April 2022; Accepted 27 April 2022
Available online 30 April 2022

applications such as catalysis [28], cytochrome accelerant [29], metal polishing agent [30], fuel cells [31], gas sensors [32], anticorrosion processes [33] and luminescence systems [34]. The rare-earth metal oxide also possesses neuroprotective, radioprotective, antimicrobial, and anti-inflammatory properties as well as potential mimicry of SOD, peroxidase, catalase, and oxidase enzymes [12,30,35,36]. The antioxidant activity of nanoceria is often attributed to its intrinsic properties, it is made of divalent oxygen anions (O^{2-}) as well as tetravalent cerium cations (Ce^{4+}) with surface trivalent cerium cations (Ce^{3+}). The rich presence of neighboring oxygen vacancies within crystal defects as well as the potential of nanoceria to reversibly switch between Ce^{3+} and Ce^{4+} states enable nanoceria to act as an antioxidant, i.e., a free radical scavenger [29,36,37].

Like most metal oxides, however, CeO_2 nanoparticles have high surface free energy and thus, the individual bare particles tend to aggregate into larger clusters, which may adversely affect their usability in certain applications, where the designated industrial conditions would result in heavily aggregated particles. For example, the surface charge of nanoceria approaches zero around the isoelectric point (IEP) and thus, unless stabilized, the catalytic performance at and around IEP is expected to be poor. Additionally, the colloidal stability is heavily dependent on other experimental conditions including temperature, ionic strength, the nature of the solvent, and the presence of polyelectrolytes or surfactants. Therefore, a full understanding of colloidal behavior is necessary for a versatile use of such materials. A common approach to overcome the particle aggregation is through the uniform decoration of these nanoparticles on larger support materials [38,39] such as clays, titania nanotubes, and graphene oxide (GO), which not only improves the poor colloidal stability, but also allows the separation the catalytic composite after the termination of the catalytic reaction.

Our previous studies have shown that antioxidant Prussian blue and MnO_2 NPs can be immobilized on larger latex particles with enhanced stability as well as better enzymatic activity [40,41]. Similar heteroaggregation processes were also utilized for the preparation of composite materials of various nano or colloidal particles [42]. Therefore, in the present work, we decorated negatively charged sulfate latex (SL) particles with cerium oxide nanoparticles (CeO_2 NPs) in attempt to design a biocatalyst with antioxidant activity (Scheme 1).

Under acidic conditions, the composites were prepared by spontaneous self-assembly of the particles (SL/Ce), while at alkaline pH, the CeO_2 NPs were initially functionalized with polyelectrolytes to adjust the charge balance prior to the heteroaggregation with SL (SPCe). The CeO_2 NPs, SPCe, and SL/Ce biocatalysts were thoroughly characterized with various methods including light scattering, spectroscopy, and electron microscopy. The horseradish peroxidase (HRP)-like activity and free radical scavenging were assessed via standard assays using 3,3′,5,5′-tetramethylbenzidine (TMB) and 2,2-diphenyl-1-picrylhydrazyl (DPPH) substrates, respectively.

2. Materials and method

2.1. Chemicals

H_2O_2 (30% m/m), HCl (37% m/m, AnalaR NORMAPUR), NaCl (99.9%), ethanol absolute (AnalaR NORMAPUR), NaOH, (≥99.3%, AnalaR NORMAPUR), ammonia (25%, AnalaR NORMAPUR), methanol (AnalaR NORMAPUR), dimethyl sulfoxide (DSMO) (AnalaR NORMAPUR) and ethylene glycol (AnalaR NORMAPUR) were obtained from VWR™. $Ce(NO_3)_3.6\,H_2O$ (99.5%) was bought from Acros Organics™, while both PDADMAC (200,000–350,000 g/mol, 20 m/m%) and 3,3′,5,5′-tetramethylbenzidine (TMB) (≥99%) were obtained from Sigma-Aldrich. The 2,2-diphenyl-1-picrylhydrazyl (DPPH) radical (95%) was bought from Alfa Aesar. Acetate buffer (pH 4.0) was prepared using glacial acetic acid (Ph.Eur./USP) and $NaCH_3COO{\cdot}3H_2O$

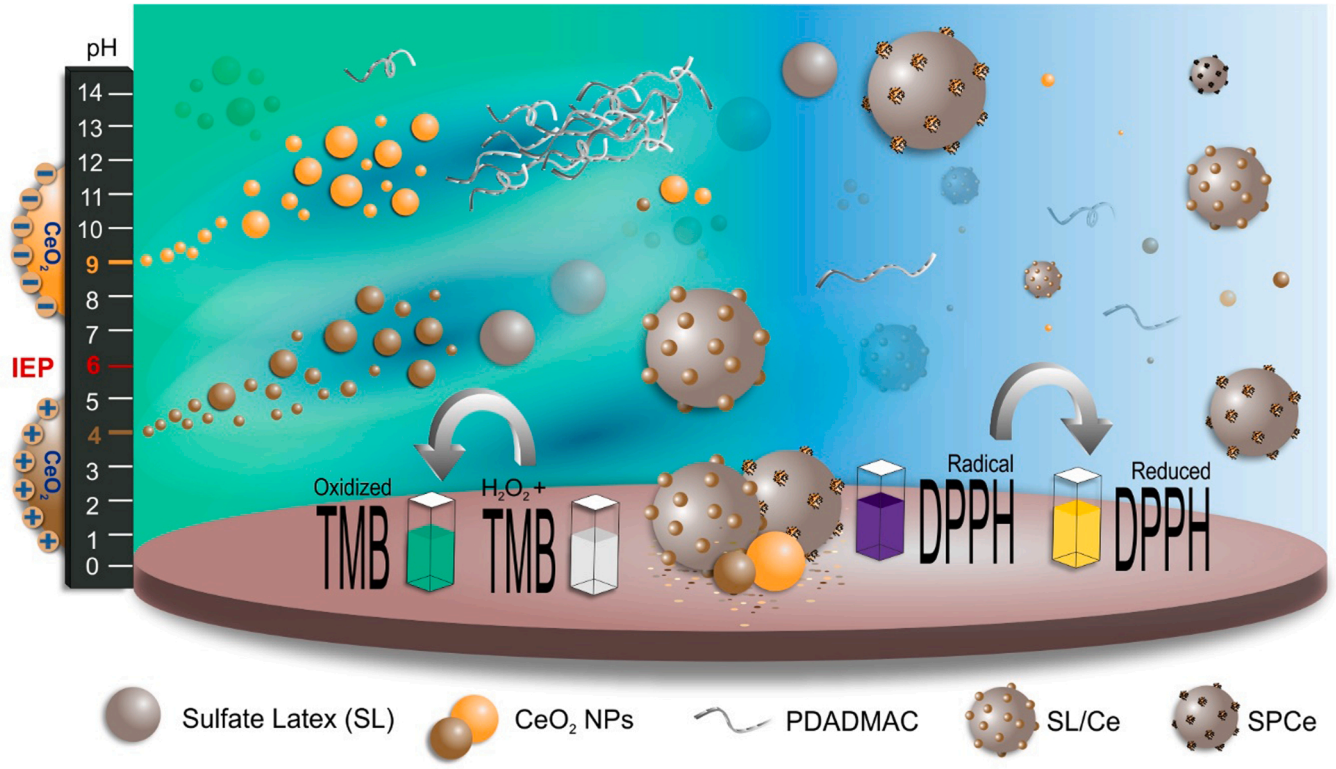

Scheme 1. Preparation of SPCe and SL/Ce at pH 9 and 4, respectively. In basic regime, CeO_2 NPs (orange) were initially functionalized with PDADMAC and were further immobilized onto SL particles (SPCe). At pH 4, CeO_2 NPs (brown) were directly immobilized onto SL particles (SL/Ce). Peroxidase-like activity as well as free radical scavenging potential are also illustrated. (For interpretation of the references to colour in this figure legend, the reader is referred to the web version of this article)

(≥99.5%), both were obtained from VWR™. Phosphate buffer (pH 7.0) was prepared using Na_2HPO_4 (≥99%, GPR RECTAPUR®) and NaH_2PO_4 (99%, anhydrous), which were purchased from VWR™ and Acros Organics™, respectively. The TRIS-HCl buffer (pH 7.0) was prepared using tris(hydroxymethyl) aminomethane (TRIS) (AnalaR NORMAPUR), purchased from VWR™. The cleaning agent Hellmanex® III was bought from Hellma. Syringe filters (PVDF-based 0.1 μm) of MILLEX-VV were used to filter the ultrapure water, which was obtained from Puranity TU 3 UV/UF+ system (VWR™). The ionic strength was adjusted with NaCl stock solutions.

2.2. Preparation of CeO_2 NPs

The glassware was carefully cleaned with Hellmanex® III and concentrated HCl solution. The CeO_2 NPs were prepared following a reported procedure [43]. Briefly, ethylene glycol 95% (7.8 mL, 0.12 mol) was dissolved in 92 mL of ultrapure water. Then, 5.16 g of Ce $(NO_3)_3{\cdot}6H_2O$ were added into the solution, followed by the addition of NH_3 to reach a pH of 9.6. The mixture was kept at 50 °C under mild stirring until a yellow solution was obtained. The yellow-colored solid product was separated by centrifugation and subsequent washing with ethanol and water. Finally, the sample was dried overnight at room temperature and the solid CeO_2 NPs were dispersed in filtered ultrapure water to obtain a 10 g/L stock.

2.3. Preparation of SL/Ce, PCe, and SPCe particles

The SL particles were obtained and fully characterized in our previous study [41]. Here, composite preparations and characterizations were carried out under acidic (pH 4.0) and basic (pH 9.0) conditions. At pH 4, the CeO_2 NPs and SL are oppositely charged and thus, the SL/Ce was heteroaggregated by mixing volumes of SL and CeO_2 NPs suspensions at the proper mass ratio. At pH 9, the adsorption of PDADMAC on CeO_2 NPs was achieved by mixing PDADMAC solutions and CeO_2 NPs dispersions to form PCe particles, which were further mixed with SL dispersions at pH 9 to prepare SPCe with the proper mass ratio. For either SL/Ce or SPCe, the optimal concentration and mass ratio of the comprising components were selected based on the colloidal properties of resulting dispersions prepared in the corresponding mass ratio. Such an optimization of the doses will be discussed later.

2.4. Material characterization

The as-prepared CeO_2 NPs were characterized by powder X-Ray Diffraction (XRD) to ensure successful preparation of the desired phase and crystallinity. The XRD patterns of CeO_2 NPs powder were recorded over a 2θ range of 20–80° and at 5°/min using Bruker D8 Advance diffractometer, equipped with a Cu Kα source (λ = 1.5406 Å).

The X-ray photoelectron spectroscopy (XPS) measurements were performed using a pass energy of 40 eV for the survey scan and 20 eV for the high-resolution scans, under a main chamber pressure range of 10^{-9}-10^{-10} mbar. The SPECS™ XPS system is equipped with a hemispherical analyzer (PHOIBOS 150 MCD 9) and Al Kα X-ray source, operated at 150 W. Adventitious carbon (284.8 eV) peak on the surface of the sample was used for charge referencing and the CasaXPS software was used for spectra evaluation.

The formation of composites (SL/Ce and SPCe) was validated via Raman spectroscopy (Bruker Senterra II Raman microscope), an average of 128 spectra was recorded at an excitation wavelength of 785 nm and 100 mW laser power, and the exposure time was set at 6 s

Further, the morphologies of CeO_2 NPs, SL/Ce, and SPCe were analyzed by transmission electron microscopy (TEM), FEI Tecnai G^2-20 X-Twin. Materials were introduced onto a copper mesh grids with carbon support (CF200-Cu, Electron Microscopy Sciences) and the loaded grids were left overnight to ensure complete evaporation of the solvent. The SL/Ce and SPCe composites morphologies were also visualized via atomic force microscopy (AFM) using Multimode Nanoscope IIIa (Digital Instruments, USA) equipped with a silicon-tip cantilever (Veeco Nanoprobe Tips) operated at resonance frequency of 275–300 kHz. Amplitude- and height-mode images were captured at room temperature in air using the tapping mode and at a scan rate of 1.0 Hz. Small aliquots of the dispersions were loaded on a newly cleaved mica (Ted Pella, Inc.) that was then left to dry at room temperature. The images were analyzed with Gwyddion software.

2.5. Light scattering

The colloidal properties of the obtained dispersions were assessed by measuring the corresponding zeta potential as well as the hydrodynamic radius at 25.0 ± 0.2 °C. The electrophoretic light scattering (ELS) was used to obtain the zeta potential with an Anton Paar Litesizer™ 500 device equipped with a laser source having a wavelength of 658 nm. The applied voltage throughout all ELS measurements was kept at 200 V. The initially measured electrophoretic mobilities were converted into zeta potentials by the Smoluchowski equation [44]. The hydrodynamic radii and aggregation rates of the particles were obtained by dynamic light scattering (DLS) using an ALV-NIBS/HPPS Particle sizer equipped with a 632.8 nm laser. The scattered light data were collected at a scatting angle of 173° and analyzed using the cumulant fit [45].

First, the dependence of zeta potential values and hydrodynamic radii of CeO_2 NPs on the pH was probed in the pH range 3–11 at constant ionic strength of 1 mM. Acidic (pH 3) and basic (pH 11) aqueous stock dispersions (50 ppm) of CeO_2 NPs were prepared. Then a series of CeO_2 NPs dispersions were obtained by mixing various volumes of the two stocks, so that the pH of the series of dispersions gradually change from 3 to 11. This procedure serves to maintain constant ionic strength of 1 mM in all the series. The pH was measured with a pH benchtop meter purchased from WTW.

The resistance of CeO_2 NPs against salt-induced aggregation was characterized at both pH 9 and 4. At each pH regime, a series of 100 ppm CeO_2 NPs dispersions was prepared at different ionic strengths, using NaCl as background salt, and the corresponding zeta potential values and aggregation rates were then measured. For the preparation of the composites, the optimal mass ratio for SL/Ce was established by comparing the zeta potential values and aggregation rates for a series of SL/Ce dispersions, where the SL was kept at 125 ppm and the CeO_2 NPs dose (mass ratio) was systematically and gradually changed between 0.1 and 10,000 mg/g (mg CeO_2 NPs/g SL) at 1 mM ionic strength and pH 4. On the other hand, the proper determination of the optimal mass ratio in SPCe was a two-step process. First, during the formation of PDADMAC-functionalized CeO_2 NPs (PCe), the proper PDADMAC dose was determined by performing the zeta potential and aggregation rate measurements for a series of PCe dispersions that were 100 ppm in CeO_2 NPs and where the PDADMAC dose was altered between 0.01 and 1000 mg/g (mg PDADMAC/g CeO_2 NPs) at 1 mM ionic strength and pH 9. Further, the optimal PCe to SL mass ratio in SPCe was determined from the results of the zeta potential and aggregation rate measurements for a series of SPCe dispersions that were 125 ppm in SL and with the PCe dose systematically altered between 0.1 and 1000 mg/g (mg PCe/g SL), again at 1 mM ionic strength and pH 9.

Zeta potential measurements were performed at 25.0 ± 0.2 °C after samples were allowed to equilibrate for 2 h at room temperature and the zeta potential value was reported as an average of 5–8 runs. On the other hand, the DLS measurements were initiated immediately upon the addition of the desired volume of CeO_2 NPs, PDADMAC, and PCe NPs during the preparation of SL/Ce, PCe, and SPCe, respectively. During time resolved DLS, the change in hydrodynamic radius over time was recorded (containing 30–100 measurement points for each sample) to obtain apparent aggregation rate constants (k_{app}) using the following equation [45]:

$$k_{app} = \frac{1}{R_h(0)} \cdot \left(\frac{dR_h(t)}{dt}\right)_{t\to 0} \quad (1)$$

where $\frac{dR_h(t)}{dt}$ is the slope of the linear fit of the hydrodynamic radius-time data points of the sample of interest and $R_h(0)$ is the hydrodynamic radius of the single particles. The colloidal stability is expressed in terms of stability ratio (W), calculated as follows [46]:

$$W = \frac{k_{app(fast)}}{k_{app}} \quad (2)$$

where $k_{app(fast)}$ is the apparent aggregation rate constant at 1.0 M ionic strength, where electrostatic forces are largely screened, and the aggregation process is solely controlled by particle diffusion. The magnitude of stability ratio is directly proportional to the colloidal stability of the corresponding dispersions. Rapidly aggregating dispersions have stability ratios close to 1 while colloidally stable ones have high stability ratio values. Additionally, aggregation half-time ($T_{1/2}$), the time required for half of the primary particles to aggregate into dimers can be calculated using the following equation [47]:

$$T_{1/2} = \frac{2}{kN_0} \quad (3)$$

where k is Smoluchowski's diffusion-controlled aggregation rate constant [45] and N_0 is the particle number concentration.

2.6. Radical scavenging activity

Antioxidant potential of CeO_2 NPs, SL/Ce and SPCe was evaluated by the DPPH (1,1-diphenyl-2-picrylhydrazyl) assay [48]. The premise of the DPPH assay is that most natural antioxidants have reactive hydrogen atoms that have the potential to reduce the violet DPPH radical into yellow reduced product, and the extent of reduction can be quantitatively studied by UV-Vis spectrophotometry. Thus, the assay is regarded as a good measure of the standard antioxidant profile. In a typical experiment, different amounts of the relevant nanozyme are added to a fixed amount of DPPH. Due to the poor aqueous solubility of DPPH, methanol serves as the solvent in the DPPH assay. Therefore, in each of the 3000 μL samples, 1800 μL of 25 ppm DPPH was added to different amounts of nanozyme so that the CeO_2 concentration (or the CeO_2 content in SL/Ce or SPCe) varied between 1 and 400 ppm. Additional volume of methanol was then added to obtain identical final volume. Upon addition of all components, the samples were rapidly vortexed and introduced into the spectrophotometer (Thermo Scientific Genesys S10 spectrophotometer). The decrease in absorbance of the DPPH radical was monitored at 517 nm using 10 mm polystyrene cuvettes (VWR). The final absorbance values at steady state were recorded. The ratio of unreacted DPPH (DPPH%) was obtained using the following equation:

$$DPPH\% = \frac{A}{A_0} 100\% \quad (4)$$

where A is the final absorbance and A_0 initial absorbance of the sample. The effective concentration (EC_{50}) is the nanozyme concentration that reduces 50% of the DPPH, which was obtained from the DPPH% versus nanozyme concentration curves. The error of precision of the method is 5%.

2.7. Horseradish peroxidase assay

The HRP-like activity was assessed via the TMB assay [49]. It is based on the oxidation of the colorless TMB substrate in the presence of H_2O_2 as well as native HRP or its mimetic nanozyme. The oxidation of TMB leads to the formation of blue product (oxidized TMB), which has a characteristic absorption peak at 652 nm. The HRP activity of CeO_2, SL/Ce, and SPCe was probed at pH 4.0, 7.0, and pH 9.0 using acetate, phosphate, and TRIS-HCl buffers, respectively. Due to its poor solubility in water, the TMB was dissolved in DMSO, and its concentration was varied between 0 and 1.5 mM, while the concentrations of H_2O_2 and the enzymatic material were kept constant. Therefore, in each of the 2000 μL samples, a varied volume of 5 mM TMB stock solution was mixed with 100 μL of 500 ppm CeO_2 NPs dispersion (or a dispersion of SL/Ce or SPCe that is 500 ppm in CeO_2 NPs), 500 μL of 200 mM buffer (acetate, phosphate, or TRIS) and a volume of ultrapure water to obtain 1900 μL sample. Finally, 100 μL of 100 mM H_2O_2 were added before the sample was immediately homogenized prior to recording the spectra. The increase in absorbance at 652 nm was recorded for 10 min. The slopes of the resulting lines represent the reaction rates (v), measured in absorbance unit per second, which can be converted to molar rates (M/s) using Beer-Lambert law, given that the optical light path is 1 cm and the molar extinction coefficient of the oxidized TMB is 39,000 $M^{-1}cm^{-1}$. Finally, the reaction rate was plotted against the corresponding TMB concentration [S], and the kinetics of the nanozyme-catalyzed TMB oxidation was assessed by fitting the rate data with the Michaelis-Menten model, expressed within the following equation:

$$v = \frac{v_{max}[S]}{K_m + [S]} \quad (5)$$

where v_{max} is the maximum concentration-independent possible reaction rate and K_m is the Michaelis-Menten constant. The latter parameter is equal to the TMB concentration corresponding to a reaction rate half that of v_{max}.

3. Results and discussion

3.1. Characterization of the CeO_2 NPs

The successful preparation of CeO_2 NPs was verified by several techniques. Fig. S1a shows the X-ray diffraction (XRD) patterns of powder CeO_2 NPs sample. Within the measured 2θ range, all the characteristic XRD reflections of CeO_2 NPs are present that match well with the standard patterns of cerium oxide (JCPDS card no. 34–0394). Similar XRD patterns were reported elsewhere [50]. Thus, all reflections can be indexed to CeO_2 with a fluorite structure (Fm3m space group) and the sharp peaks indicate that the formed particles were highly crystalline.

In addition, surface chemical composition of CeO_2 NPs was explored with XPS. The XPS survey scan, shown in Fig. S1b, reveals the occurrence of Ce, C, O, and Fe elements on the surface of the sample, with the presence of Fe attributed to the sample holder. Similar spectra for nanoceria were reported in literature [50,51]. The quantitative XPS composition analysis resulted in the following surface chemical composition of the sample: 14.8 at% Ce, 24.8 at% C, and 60.4 at% O (Table S1, see Supplementary material (SM)). In addition, the high-resolution Ce 3d core-level spectrum (Fig. S2a) shows two sets of multiplets. The multiplet comprising of (v^0, v′) and (u^0, u′) are related to surface Ce(III), while the multiplet of (v, v″, and v‴) and (u, u″, and u‴) peaks refer to surface Ce(IV) [51,52]. The exact binding energy values of the ten peaks along with the reference values are listed in Table S2 and indicate a mixed valence state of Ce(III)/Ce(IV). The contribution of Ce (III) to the overall composition is ~15 at%, which signals a sub-stoichiometric oxide surface [53]. The high-resolution C 1 s spectrum in Fig. S2b can be attributed to the presence of adventitious carbon on the surface of the CeO_2 NPs. The peaks at 286.37 eV and 298.07 eV correspond C–OH and O–C═O functionalities, respectively while the peak at 284.82 eV refers to C–C/C–H states. The resolved high-resolution O 1 s spectrum is presented in Fig. S2c. Two peaks at 529.62 eV and 531.62 eV correspond to lattice oxide and surface hydroxide, respectively. Their position and relative contribution suggest the prevalence of hydroxide species on the sample surface, as reported elsewhere [54]. The lattice oxide is 43.7% of the overall O 1 s peak and

thus, the surface stoichiometry is $CeO_{1.8}$, which is close to CeO_2.

Fig. 1a shows the Raman spectrum for CeO_2 NPs. The intense peak at 462 cm^{-1} is attributed to the symmetrical stretching mode of the Ce–O vibration. The inset graph further shows the peak at 462 cm^{-1} in the Raman shift range of 350–550 cm^{-1}, which is characteristic for CeO_2 [55,56]. Moreover, the UV-Vis spectrum, shown in Fig. 1b and recorded in the 250–550 nm wavelength range, shows a broad peak around 300 nm, which is characteristic for CeO_2, as reported in the literature [57,58]. Additionally, the CeO_2 NPs morphology was analyzed via TEM and high-resolution TEM (HR-TEM). Fig. 1c shows a TEM image of the prepared CeO_2 NPs, the particles are characterized by well-established boundaries with semi-cubic morphology. The aggregated state of CeO_2 NPs is attributed to the drying process during sample preparation. The HR-TEM image (Fig. 1d) of CeO_2 NPs shows differently oriented crystal fringes. The squared region in the HR-TEM image appears to have several distinct and superimposed lattice spacings and thus, fast Fourier-transform (FFT) analysis was carried out. The extracted pattern, shown in Fig. 1e, indicates the presence of three lattice spacings, which were obtained by inverse FFT analysis. The three inverse FFT images and the corresponding lattice spacing values are shown in the inset images of Fig. 1e. The obtained ~0.25 nm lattice spacing correspond to that obtained from the (200) peak, while ~0.36 nm is close to the one obtained from the (111) peak, which is typically ~0.31 nm, but cannot be unambiguously assigned. The lattice spacing of ~0.75 nm corresponds to a 2θ value outside the range of the utilized XRD instrument, and thus could not be unambiguously assigned as well.

The pH-dependent surface charge of ceria materials is known [59], therefore, zeta potential values and hydrodynamic radii of CeO_2 NPs were determined at different pH conditions (Fig. S3). In highly acidic media, CeO_2 NPs have high positive charge due to the protonated surface OH groups reaching 32.7 ± 0.7 mV at pH 4. As the pH increases, however, the extent of protonation and thus, the zeta potential values decrease. At the IEP (pH ~6.17) CeO_2 NPs undergo charge reversal, where the emerging negative charge originates from the deprotonation of surface OH groups. Its extent increases as the pH becomes more basic, which is reflected in the high corresponding zeta potential values, reaching − 29.2 ± 1.0 mV at pH 9. On the other hand, the increase in the magnitude of zeta potential is accompanied by decrease in the hydrodynamic radii reaching as low as 181.2 ± 24.2 nm and 180.0 ± 31.4 nm at pH 4.0 and 9.0, respectively. In the pH range 5.5–8.5, the zeta potential drops to values between − 10 and 10 mV, accompanied by a sudden and significant rise in hydrodynamic radii, indicating rapidly aggregating dispersions. Low zeta potential of particles indicates weak electrostatic repulsive forces and leads to subsequent formation of large aggregates due to attractive van der Waals forces.

3.2. Homoaggregation of CeO_2 NPs

The salt-induced aggregation of CeO_2 NPs was also assessed at different ionic strengths both at pH 4 and pH 9. Eq. (2) was used to obtain the stability ratio at distinct ionic strengths. As shown in Fig. S4a, at pH 4 regime, increasing the salt content gradually decreases the stability ratio of CeO_2 NPs dispersions until it reaches unity at a NaCl concentration of 60.0 mM. This value is the so-called critical coagulation concentration (CCC), at which the system changes from slow aggregation to fast aggregation. Further addition of NaCl at or higher than 60 mM does not change the stability ratio. According to the DLVO theory, the addition of salt reduces the Debye length of the electric double layer around CeO_2 NPs, and the resulting surface charge screening leads to weakening of the repulsive electrical double layer (EDL) forces and hence, CeO_2 NPs undergo rapid aggregation under the influence of the van der Waals forces [60].

Similar conclusions are reached when the zeta potential values of CeO_2 NPs at different ionic strengths are measured. Accordingly, the CeO_2 NPs possess high zeta potential indicating strong EDL repulsion at low ionic strength owing to the deprotonated OH groups. As the ionic strength is raised, the surface charge on CeO_2 NPs become increasingly screened, which is reflected in gradual drop in the zeta potential, i.e., in weakening of electrostatic repulsion.

The tendencies for CeO_2 NPs at pH 9 were the same, as shown in Fig. S4b. The stability ratio as well as the magnitude of zeta potential gradually decreased with the increase in the ionic strength as a result of

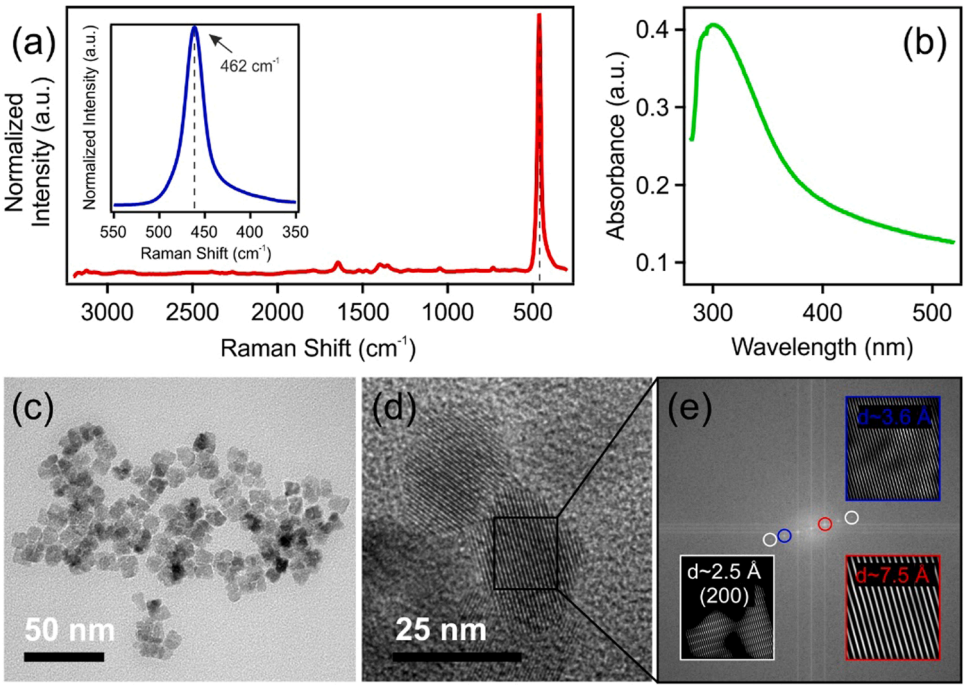

Fig. 1. (a) Raman spectrum of bare CeO_2 NPs (Inset graph: the magnified peak at 462 cm^{-1}), (b) the UV-Vis absorption spectrum of bare CeO_2 NPs, (c) TEM image of CeO_2 NPs, (d) HR-TEM image of CeO_2 NPs, (e) the extracted pattern, obtained by FFT analysis, of the squared section in the HR-TEM image. The inset images and lattice spacing values are obtained by inverse FFT analysis of the FFT pattern, using ImageJ software.

charge screening and subsequent aggregation [60]. However, the CCC is located at 5.5 mM, which indicates significantly lower colloidal stability of CeO_2 NPs at pH 9 owing to the lower magnitude of zeta potential, compared to pH 4. Thus, in acidic pH conditions, the CeO_2 NPs possess higher surface charge and stronger resistance against salt-induced aggregation, compared to alkaline pH conditions. Additionally, the mechanism of CeO_2 NPs aggregation aligns with the prediction of the DLVO theory at both pH regimes, similar to other colloidal systems of charged particles dispersed in salt solutions [39,47,61]. Table S3 shows the hydrodynamic radii and zeta potential values along with other colloidal properties of CeO_2 NPs at pH 4 and pH 9.

3.3. Heteroaggregation of CeO_2 NPs with SL

In our previous work, we characterized the SL particles by probing the aggregation tendency of SL at different SL concentrations and 1.0 M ionic strength as well as at different pH conditions in attempt to optimize the experimental conditions for later aggregation rate measurements [41]. Setting the background salt concentration at 1.0 M screens electrostatic repulsive forces, which leads to rapid aggregation according to the DLVO theory. Our previous results indicated that applying 125 ppm SL provides sufficient intensity of scattered light, but not high enough to trigger higher rank aggregates [41]. Therefore, here, the concentration of negatively charged SL was kept at 125 ppm as the dose of oppositely charged CeO_2 NPs (in mg CeO_2 NPs/g SL) was gradually adjusted. Since the intensity of scattered light is directly proportional to the 6th power of the particle size [46], the scattered light thus originates mostly from SL particles rather than CeO_2 NPs due to the considerable size difference.

Fig. 2 shows the zeta potential and stability ratio values of SL/Ce composite at different CeO_2 NPs doses. At low CeO_2 NPs doses, the SL/Ce particles maintained high negative charge and thus, high stability ratio. However, as the dose was raised, the magnitude of the overall negative charge as well as the stability ratio decreased indicating significantly increased adsorption of CeO_2 NPs on the SL particles. Around the IEP, which occurred at 100 mg CeO_2 NPs/g SL, the zeta potential of SL/Ce particles approached zero and the stability ratio of the corresponding dispersion dropped to 1, indicating heavily aggregating SL/Ce composite particles. Higher CeO_2 NPs doses led to the formation of increasingly overall positively charged SL/Ce particles with increasing stability ratio. The zeta potential reached a maximum value at and beyond a CeO_2 NPs dose of 1000 mg CeO_2 NPs/g SL, the onset of the adsorption saturation plateau (ASP), where SL particles became saturated with adsorbed CeO_2 NPs.

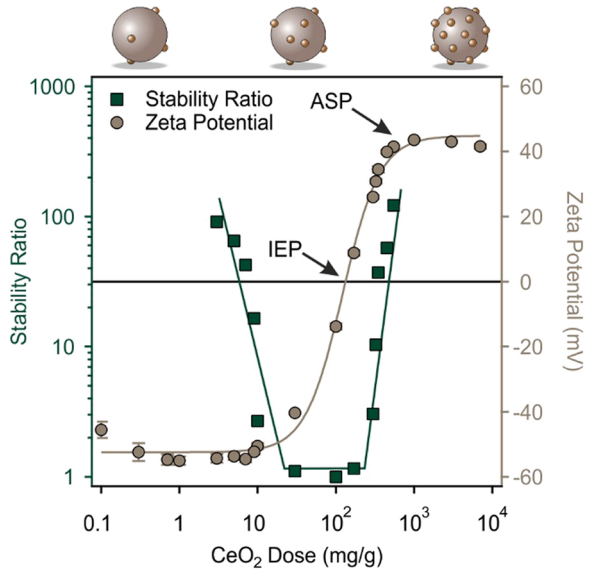

Fig. 2. Stability ratio (squares) and zeta potential (circles) values of dispersions of SL at different concentrations of CeO_2 NPs at pH 4 and 1 mM ionic strength. The concentration of SL was fixed at 125 ppm and the mg/g unit refers to mg CeO_2 NPs per one gram of SL. The solid lines serve as eye guidance only and the graphical representation of SL/Ce composite is not to scale.

Since the experimental conditions were set so that individual CeO_2 NPs and SL are highly charged, the homoaggregation is negligible. Moreover, in particle-particle systems, two regimes of interparticle forces are established. First, electrostatic attraction as well as van der Waals forces between SL and CeO_2 NPs, which drive the heteroaggregation and give rise to SL/Ce composite particles. Second, EDL forces and attractive van der Waals forces exist among the individual SL/Ce hybrid particles. In the second regime, electrostatic repulsion forces dominate at low and high CeO_2 NPs doses and provide stable hybrid dispersion, while the van der Waals forces are significant around the IEP, where the overall charge on the SL/Ce particles approaches zero. Thus, hybrid particles in particle-particle systems are formed. Similar patterns were also obtained in other studies [40,61].

The immobilization of CeO_2 NPs on SL at pH 4 was visualized by TEM and AFM techniques. The TEM images in Fig. 3(a, b) clearly indicate the successful immobilization of CeO_2 NPs on SL particles, where the CeO_2 NPs dose was set at 1000 mg/g (the onset of the ASP in Fig. 2). The resulting SL/Ce composite is characterized by uniform distribution of the CeO_2 NPs on the SL particle surface. Similar morphology is observed with the AFM imaging technique. Fig. 3(c,d) shows the amplitude and height AFM images as well as the height profiles of SL/Ce system (Fig. 3e). These images provide direct evidence that positively charged CeO_2 NPs were successfully and firmly immobilized on the surface of SL particles.

3.4. PDADMAC functionalization of CeO_2 NPs

At pH 9, CeO_2 NPs are negatively charged, and thus, the immobilization of CeO_2 NPs onto the similarly charged SL particles by electrostatic attraction requires surface modification of the CeO_2 NPs that gives rise to overall positive surface charge. Thus, the CeO_2 NPs were surface modified with PDADMAC polyelectrolyte. Such charged macromolecules are known for their strong adsorption on oppositely charged surfaces [41,62]. Therefore, the surface of CeO_2 NPs is expected to have an overall positive charge upon addition of proper amount of PDADMAC. The precise PDADMAC dose was tuned to obtain stable dispersions of functionalized CeO_2 NPs (PCe). The zeta potentials of CeO_2 NPs, determined at different PDADMAC doses, are shown in Fig. S5.

The addition of PDADMAC gradually reduced the negative charge on CeO_2 NPs until enough PDADMAC was added to fully neutralize the negative charge of CeO_2 NPs at the IEP, at which the zeta potential of CeO_2 NPs is zero. The IEP was located around a dose of 1 mg PDADMAC/g CeO_2 NPs, and larger PDADMAC doses caused charge reversal leading to positively charged PCe particles. The zeta potential reached a maximum value at the onset of the ASP, that occurred around at 10 mg/g dose, where the surface of CeO_2 NPs became saturated with PDADMAC, and further added polyelectrolytes remain dissolved in the solution, and the corresponding magnitude of zeta potential remained constant.

Besides, the stability ratios were measured under the same experimental conditions to assess the colloidal stability of the PCe dispersions. As shown in Fig. S5, changes in the stability ratios occurred with the gradual decrease in zeta potential values. Like the SL/Ce system at pH 4, high magnitude of zeta potential is accompanied by high stability ratio, while significant destabilization occurs when the PDADMAC doses correspond to those around the IEP, where the stability ratios drop to unity, and the dispersion undergoes heavy PCe particle aggregation. Such pattern is commonly observed in oppositely charged particle-polyelectrolyte systems [62–64]. Unlike particle-particle systems, however, non-DLVO-type forces may play a role in the colloidal stability of particle-polyelectrolyte systems. Accordingly, repulsive steric as well as attractive bridging and patch-charge forces may play a part along

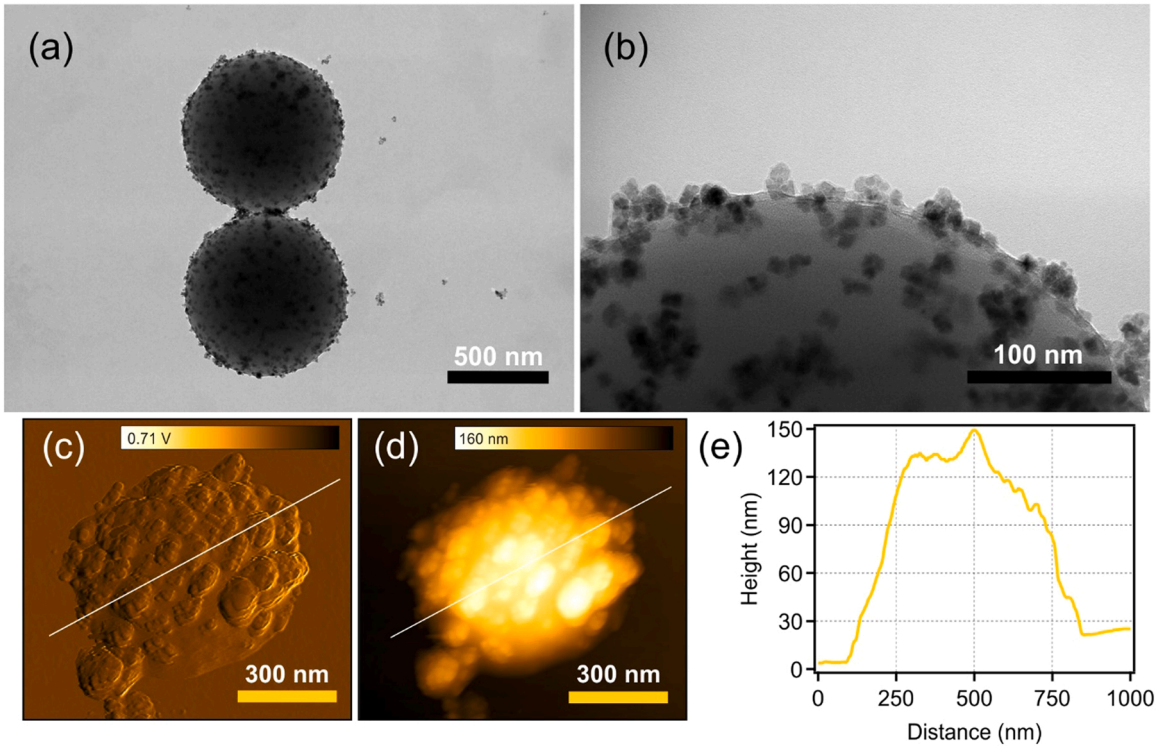

Fig. 3. (a,b) TEM images, (c) amplitude and (d) height AFM images of SL/Ce composite deposited on a mica substrate along with (e) the height profiles taken along the indicated white lines.

with DLVO forces during homoaggregation of the PCe particles [63,65]. Lastly, since the CeO_2 NPs surface saturation occurred at PDADMAC doses around 30 mg/g, the functionalized CeO_2 NPs prepared at 40 mg PDADMAC/g CeO_2 NPs dose are denoted as PCe. They possess high positive charge and high stability ratio, which render them suitable for heteroaggregation with negatively charged SL.

3.5. Heteroaggregation of PCe with SL

Fig. 4 shows the zeta potential and stability ratio values of SPCe at different PCe (prepared at 40 mg PDADMAC/g CeO_2 NPs) doses. The SPCe particles maintained high negative charge and thus, high stability ratio at low PCe doses. As the dose was increased, however, the magnitude of the negative charge as well as the stability ratio decreased indicating increased adsorption of PCe on the SL particles. Around the IEP, which occurred at 16 mg/g dose, the zeta potential of SPCe particles approached zero and the stability ratio of the corresponding dispersion dropped to unity indicating highly aggregating SPCe particles. Higher PCe doses led to the formation of increasingly overall positively charged SPCe particles with increasing stability ratio. The zeta potential reached a maximum value at and beyond a PCe dose of 55 mg PCe/g SL, the onset of the ASP, where SL particles became saturated with adsorbed PCe. Such particle-polyelectrolyte-particles are far less commonly reported, compared to simpler polyelectrolyte-particle or particle-particle systems [41]. However, the tendencies in mobilities and stability ratios resemble those of the SL/Ce (Fig. 2).

The morphology of SPCe composite, formed at pH 9, was visualized with TEM and AFM techniques. The TEM images in Fig. 5(a, b, c) clearly show immobilization of PDADMAC-functionalized CeO_2 NPs onto SL particles. Fig. 5(d, e) represents the amplitude and height AFM images of SPCe system along with the height profile (Fig. 5 f). The PDADMAC dose was 40 mg/g (the onset of ASP in Fig. S5), and the CeO_2 NPs dose was 200 mg/g (the onset of ASP in Fig. 4). It is important to note that the SL particles in the SPCe composite are not covered to the same extent as the SL particles in SL/Ce composite as shown in the TEM images in Fig. 3,

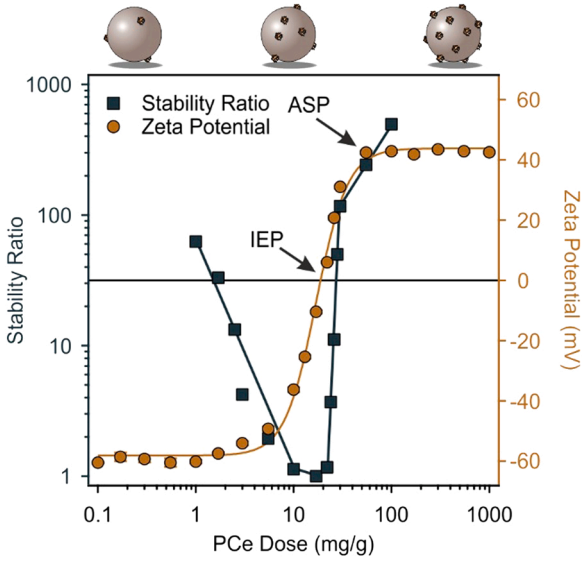

Fig. 4. Stability ratio (squares) and zeta potential (circles) values of SL particles in the presence of PCe at different doses at pH 9 and 1 mM ionic strength. The concentration of SL was fixed at 125 ppm, and the PCe composition was maintained at 40 mg PDADMAC/g CeO_2 NPs. The mg/g unit refers to mg PCe per one g of SL. The solid lines serve as eye guidance only and the graphical representation of SPCe is not to scale.

even though the CeO_2 NPs and PCe doses used for imaging correspond to doses at the onset of saturation plateau in both systems. The potential reason is that the PDADMAC is highly effective in the charge modification and neutralization, as evident in the IEP values of the SL/Ce and SPCe systems, which are 100 mg/mg and 10 mg/g, respectively. For the same SL concentration (125 ppm), the presence of PDADAMC significantly lowered the IEP dose by one order of magnitude and thus, less

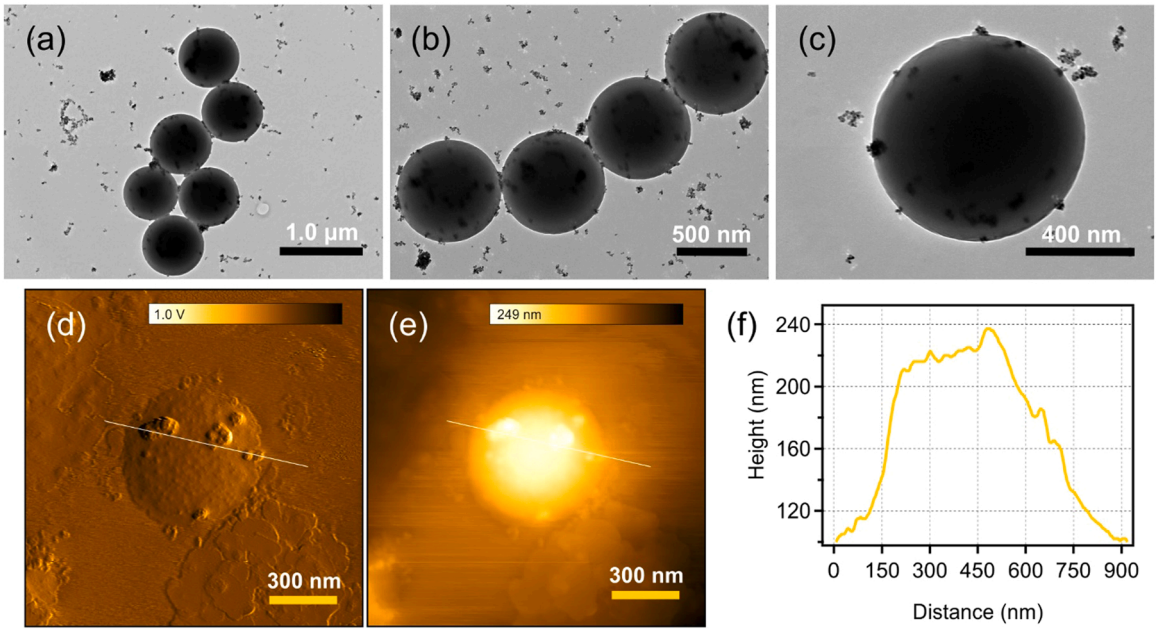

Fig. 5. (a,b,c) TEM images of SPCe composite at different magnification. (d) Amplitude and (e) height AFM images of SPCe composite deposited on a mica substrate along with (f) the height profile curve taken along the indicated white lines. In the composite dispersion, the PDADMAC dose was 40 mg/g (the onset of ASP in Fig. S5) and the CeO_2 NPs dose was 200 mg/g (the onset of ASP in Fig. 4).

CeO_2 NPs are required to cause charge reversal in the SPCe system. Therefore, the SPCe particles are expected to be less decorated with functionalized CeO_2 NPs compared to the extent of SL/Ce composites decoration with bare CeO_2 NPs.

The immobilization of CeO_2 NPs and PCe particles on SL was further proved by Raman spectroscopy. In addition to Raman spectrum of CeO_2 NPs, the individual Raman spectra of SL and PDADMAC dispersions as well as those of SL/Ce and SPCe were recorded (Fig. S6). The characteristic peaks in the Raman spectrum of SL at 620 cm^{-1} and 1000 cm^{-1} was attributed to different deformation mode bands of the aromatic ring, while C–C stretches (1150–1200 cm^{-1}) and the ring skeletal stretch (1602 cm^{-1}) were identified as well. These peaks of the individual components agree very well with those reported elsewhere in the literature [66]. The peaks in the Raman spectrum of PDADMAC were identified as the N–C stretches (790 cm^{-1}) and the CH_3 stretching vibration (1449 cm^{-1}) [67]. The vibrational modes that give rise to Raman peaks are assigned in Table S4.

As Fig. S6 shows, Raman spectra of SL/Ce and SPCe composites contain all the characteristic Raman peaks of SL (indicated by circles) and the lone peak of CeO_2 NPs (indicated by squares) in the same peak positions, compared to the spectra of the individual materials. The immobilization, however, resulted in weakening of peak intensity of CeO_2 NPs, but had no effect on the intensities of SL peaks. An interesting observation is the absence of characteristic PDADMAC peaks in the spectrum of SPCe due to the 10 times lower Raman intensity of PDADMAC (the actual intensity values are labeled on the graph) [67]. Accordingly, to probe the antioxidant activity, these colloidally stable composites have been prepared at 1000 and 200 mg/g (mg CeO_2 NPs/g SL) for SL/Ce and SPCe systems, respectively.

3.6. Antioxidant activity

The radical scavenging potential of the CeO_2 NPs, SL/Ce, and SPCe particles was assessed via standard DPPH assay, based on the reduction of the purple DPPH radicals to yellow molecules. The decrease in absorbance of the violet DPPH radical was monitored at 517 nm and the percentage of unreacted DPPH (abbreviated as DPPH%) was obtained using Eq. (4). Fig. 6 shows the DPPH% as a function of the nanozyme concentration (referring to bare CeO_2 NPs or the CeO_2 NPs content in either SPCe or SL/Ce). Accordingly, DPPH% decreased with the increase in nanozyme concentration, indicating less radicals remain, when more nanozymes are present.

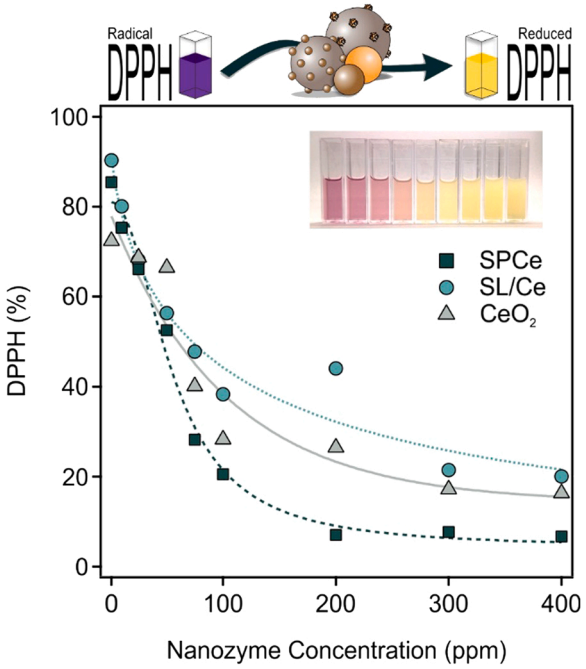

Fig. 6. Radical scavenging activity of CeO_2 NPs, SL/Ce, and SPCe. The DPPH concentration in all samples was kept at 15 ppm. The solid/dashed lines only serve as eye guidance and DPPH% was calculated according to Eq. (4). The inset image shows that the intensity of the yellow color increases with the increased nanozyme concentration. (For interpretation of the references to colour in this figure legend, the reader is referred to the web version of this article)

Fig. 6 also shows that while SL/Ce and CeO_2 NPs have comparable

radical scavenging potential, SPCe has better antioxidant activity, as indicated by the steeper decrease. The enhanced antioxidant performance can be attributed to the less aggregated state or greater accessible particle area of the immobilized PCe compared to the bare CeO_2 NPs, since the latter are more likely undergo aggregation, which leads to reduced antioxidant activity because of the increased number of unavailable active sites. The calculated EC_{50} values of bare CeO_2 NPs and the composites are shown in Table S5.

The CeO_2 NPs were also found to exhibit HRP-like activity. As mentioned earlier, the HRP assay is based on the oxidation of the colorless TMB substrate in the presence of H_2O_2 as well as native HRP or its mimetic nanozyme such as CeO_2 NPs, where the oxidation of TMB leads to the formation of a blue product (oxidized TMB). Native peroxidase or its mimetic nanozymes catalyzes the reduction of H_2O_2 to water in the presence of some hydrogen donor substrate such as TMB substrate. Fig. 7 demonstrates the HRP-like activity of CeO_2 NPs and shows that the oxidized TMB has a characteristic wavelength of 652 nm.

In the TMB/CeO_2 combination, no absorption peak was observed, and the reaction mixture remained colorless indicating no oxidation of TMB had taken place (Fig. 7 inset: cuvette α). For TMB/H_2O_2 mixture, a very weak peak appeared indicating an insignificant amount of TMB underwent oxidation, and the mixture exhibited a very pale blue color (Fig. 7 inset: cuvette β). The uncatalyzed oxidation of TMB may be attributed to the slow decomposition of the H_2O_2 substrate into hydroxyl radicals that lead to TMB oxidation. However, when the three components were present, i.e., TMB, H_2O_2, and CeO_2, the mixture exhibited a deep blue color (Fig. 7 inset: cuvette γ) and had a strong absorption peak at 652 nm indicating substantial oxidation of TMB occurred, which demonstrates that CeO_2 NPs possess peroxidase-like activity.

Fig. S7a shows the reaction rate of TMB oxidation at various TMB concentrations at 25 ppm CeO_2 NPs as well as 5 mM H_2O_2. The TMB concentration was changed between 0 and 1.5 mM, rate measurements with higher TMB levels were not feasible due to poor solubility and precipitation of TMB during the measurement. Further, the obtained experimental rate data for CeO_2 NPs, SL/Ce, and SPCe were fitted with the Michaelis-Menten kinetic model (Eq. 5), as Fig. S7a shows. The resulting Michaelis-Menten parameters are listed in Table S5. The maximum velocity (v_{max}) is the maximum experimentally observed rate that remains unchanged regardless of the TMB concentration, this possibly occurs as a result of saturation of the catalytic sites. On the other hand, Michaelis-Menten constant (K_m) is the TMB concentration that corresponds to half v_{max}. It is a measure of the affinity between the catalyst and the substrate, where a lower K_m value indicates a higher affinity between the enzyme-like material and the substrate. Interestingly, K_m for SL/Ce (0.200 mM) is nearly two times lower than that for bare CeO_2 NPs (0.359 mM) indicating stronger affinity of TMB towards immobilized CeO_2 NPs. On the other hand, the K_m for SPCe (0.467 mM) is comparable to that of bare CeO_2 NPs and thus, the TMB has similar affinities towards both SPCe and bare CeO_2 NPs.

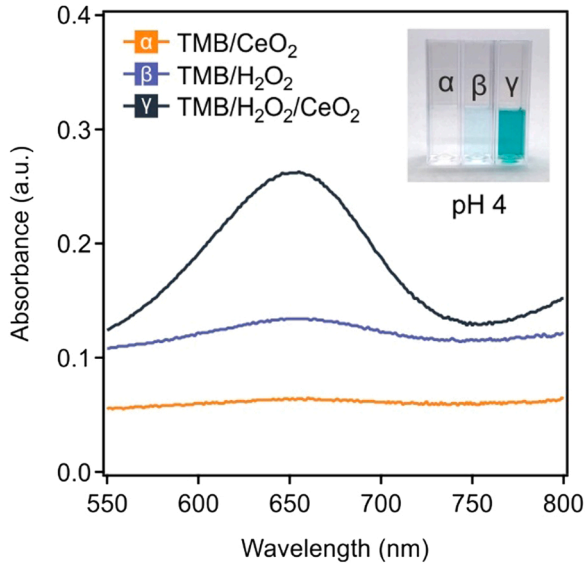

Fig. 7. The UV-Vis spectra of TMB/CeO_2 (orange/α spectrum), TMB/H_2O_2 (blue/β spectrum) and TMB/H_2O_2/CeO_2 (black/γ spectrum). The inset graphics shows the real samples, measured at pH 4. Samples prepared with the following relevant concentrations: 1 mM TMB, 25 ppm CeO_2 NPs, and 5 mM H_2O_2.

The trends in v_{max} of the composites also indicate either similar (SL/Ce) or higher (SPCe) v_{max} compared to bare CeO_2 NPs. Thus, the SL immobilization and PDADMAC functionalization of CeO_2 NPs not only had no effect on the HRP-like activity, but rather resulted in lower K_m and higher v_{max} for SL/Ce and SPCe, respectively. Further, Table S5 shows that both bare CeO_2 NPs and SL/Ce have lower K_m than native HRP, while SPCe has comparable K_m [68]. In addition, the HRP-like activity of CeO_2 NPs was further evaluated at pH 7 and pH 9. Fig. S7b shows that the CeO_2 NPs do not possess HRP-like activity in neutral and alkaline conditions, this trend for pH-dependent HRP activity for TMB has been reported in the literature [69,70]. Thus, the kinetics of the nanoceria-catalyzed oxidation reaction of TMB was only evaluated at pH 4 (Fig. S7a). Accordingly, the results of HRP and DPPH assays suggest that the SPCe and SL/Ce hybrids possess remarkable antioxidant potential as well as HRP-like activity that is comparable to native enzyme. These features, coupled with the colloidal and structural stability of the composites, render them versatile materials for industrial applications, where cheap and stable enzyme alternatives are desired.

4. Conclusions

Composites of CeO_2 NPs were formulated by immobilization onto negatively charged sulfate latex support particles via heteroaggregation under the influence of electrostatic attraction forces. In acidic regime, the positively charged CeO_2 NPs were directly immobilized onto SL (SL/Ce composite), while surface functionalization of negatively charged CeO_2 NPs with PDADMAC polyelectrolyte was necessary at alkaline conditions to induce charge reversal and enable subsequent immobilization onto SL (SPCe composite). Microscopy techniques, however, showed lower surface distribution of nanoceria catalytic centers in SPCe. Depending on the mass ratio of bare and functionalized CeO_2 NPs, negatively or positively charged hybrid particles could be obtained with high colloidal stability as a result of strong electrostatic repulsion. At mass ratios corresponding to that at the IEP, however, the overall charge on the hybrid particles approached zero, resulting in significant aggregation under the influence of van der Waals forces. Both composites showed excellent potential as radical scavengers and possessed remarkable HRP-like activity with Michaelis constants comparable to the native enzyme. These findings demonstrate that SL/Ce and SPCe composites are promising antioxidants in heterogeneous systems due to the accumulation of catalytic centers in small volumes, the ease of separation from the reactions mixture, and the high colloidal stability.

CRediT authorship contribution statement

Nizar B. Alsharif: Investigation, Writing – original draft, Methodology. **Gergely F. Samu**: Software, Methodology. **Szilárd Sáringer**: Validation, Methodology. **Adél Szerlauth:** Data curation; Formal analysis. **Dóra Takács:** Methodology, Visualization. **Viktoria Hornok:** Supervision, Investigation. **Imre Dékány:** Writing – review & editing, Resources. **Istvan Szilagyi**: Conceptualization, Supervision, Writing – review & editing, Project administration, Resources.

Declaration of Competing Interest

The authors declare that they have no known competing financial interests or personal relationships that could have appeared to influence

the work reported in this paper.

Acknowledgments

The research was financially supported by the Eötvös Lóránd Research Network/Hungarian Academy of Sciences through the Lendület program (96130) and by project no. TKP2021-NVA-19, which has been implemented with the support provided by the Ministry of Innovation and Technology of Hungary from the National Research, Development and Innovation Fund, financed under the TKP2021-NVA funding scheme. The support from the University of Szeged Open Access Fund (5739) is gratefully acknowledged.

Supplementary material

Supplementary data to this article can be found online. Material composition data, deconvolution of XPS peaks, Raman shift values, dispersions characteristics as well as functionalization and enzymatic activity data.

Appendix A. Supporting information

Supplementary data associated with this article can be found in the online version at doi:10.1016/j.colsurfb.2022.112531.

References

[1] G. Carrea, S. Riva, Properties and synthetic applications of enzymes in organic solvents, Angew. Chem. Int. Ed. 39 (2000) 2226–2254.
[2] A.A. Vernekar, D. Sinha, S. Srivastava, P.U. Paramasivam, P. D'Silva, G. Mugesh, An antioxidant nanozyme that uncovers the cytoprotective potential of vanadia nanowires, Nat. Commun. 5 (2014) 5301.
[3] G. Fuhrmann, A. Grotzky, R. Lukic, S. Matoori, P. Luciani, H. Yu, B.Z. Zhang, P. Walde, A.D. Schluter, M.A. Gauthier, J.C. Leroux, Sustained gastrointestinal activity of dendronized polymer-enzyme conjugates, Nat. Chem. 5 (2013) 582–589.
[4] J. Chapman, A.E. Ismail, C.Z. Dinu, Industrial applications of enzymes: recent advances, techniques, and outlooks, Catalysts 8 (2018) 238.
[5] W.H. Liew, M.H. Hassim, D.K.S. Ng, Review of evolution, technology and sustainability assessments of biofuel production, J. Clean. Prod. 71 (2014) 11–29.
[6] S. Raveendran, B. Parameswaran, S.B. Ummalyma, A. Abraham, A.K. Mathew, A. Madhavan, S. Rebello, A. Pandey, Applications of microbial enzymes in food industry, Food Technol. Biotechnol. 56 (2018) 16–30.
[7] D.P. Riley, Functional mimics of superoxide dismutase enzymes as therapeutic agents, Chem. Rev. 99 (1999) 2573–2587.
[8] O. Kirk, T.V. Borchert, C.C. Fuglsang, Industrial enzyme applications, Curr. Opin. Biotechnol. 13 (2002) 345–351.
[9] Y.H. Lin, J.S. Ren, X.G. Qu, Catalytically active nanomaterials: a promising candidate for artificial enzymes, Acc. Chem. Res. 47 (2014) 1097–1105.
[10] R.F. Zhang, X.Y. Yan, K.L. Fan, Nanozymes inspired by natural enzymes, Acc. Mater. Res. 2 (2021) 534–547.
[11] L.L. Dugan, J.K. Gabrielsen, S.P. Yu, T.S. Lin, D.W. Choi, Buckminsterfullerenol free radical scavengers reduce excitotoxic and apoptotic death of cultured cortical neurons, Neurobiol. Dis. 3 (1996) 129–135.
[12] H. Wei, E.K. Wang, Nanomaterials with enzyme-like characteristics (nanozymes): next-generation artificial enzymes, Chem. Soc. Rev. 42 (2013) 6060–6093.
[13] J.J.X. Wu, X.Y. Wang, Q. Wang, Z.P. Lou, S.R. Li, Y.Y. Zhu, L. Qin, H. Wei, Nanomaterials with enzyme-like characteristics (nanozymes): next-generation artificial enzymes (II), Chem. Soc. Rev. 48 (2019) 1004–1076.
[14] L. Valgimigli, A. Baschieri, R. Amorati, Antioxidant activity of nanomaterials, J. Mat. Chem. B 6 (2018) 2036–2051.
[15] K. Li, J. Yang, J.L. Gu, Spatially organized functional bioreactors in nanoscale mesoporous MOFs for cascade scavenging of intracellular ROS, Chem. Mat. 33 (2021) 2198–2205.
[16] M. Moglianetti, E. De Luca, P.A. Deborah, R. Marotta, T. Catelani, B. Sartori, H. Amenitsch, S.F. Retta, P.P. Pompa, Platinum nanozymes recover cellular ROS homeostasis in an oxidative stress-mediated disease model, Nanoscale 8 (2016) 3739–3752.
[17] L.F. Wang, Y. Li, L. Zhao, Z.J. Qi, J.Y. Gou, S. Zhang, J.Z. Zhang, Recent advances in ultrathin two-dimensional materials and biomedical applications for reactive oxygen species generation and scavenging, Nanoscale 12 (2020) 19516–19535.
[18] C. Liu, Y.Y. Yan, X.W. Zhang, Y.Y. Mao, X.Q. Ren, C.Y. Hu, W.W. He, J.J. Yin, Regulating the pro- and anti-oxidant capabilities of bimetallic nanozymes for the detection of Fe^{2+} and protection of Monascus pigments, Nanoscale 12 (2020) 3068–3075.
[19] A. Liese, L. Hilterhaus, Evaluation of immobilized enzymes for industrial applications, Chem. Soc. Rev. 42 (2013) 6236–6249.
[20] J.S. Niu, Y.H. Sun, F.M. Wang, C.Q. Zhao, J.S. Ren, X.G. Qu, Photomodulated nanozyme used for a gram-selective antimicrobial, Chem. Mat. 30 (2018) 7027–7033.
[21] E. Kuah, S. Toh, J. Yee, Q. Ma, Z.Q. Gao, Enzyme mimics: advances and applications, Chem. Eur. J. 22 (2016) 8404–8430.
[22] Y.N. Li, J. Sun, W. Mao, S. Tang, K. Liu, T. Qi, H.M. Deng, W. Shen, L.Z. Chen, L. M. Peng, Antimony-doped tin oxide nanoparticles as peroxidase mimics for paper-based colorimetric detection of glucose using smartphone read-out, Microchim. Acta 186 (2019) 403.
[23] L.J. Huang, W.X. Zhu, W.T. Zhang, K. Chen, J. Wang, R. Wang, Q.F. Yang, N. Hu, Y. R. Suo, J.L. Wang, Layered vanadium(IV) disulfide nanosheets as a peroxidase-like nanozyme for colorimetric detection of glucose, Microchim. Acta 185 (2018) 7.
[24] Y.J. Song, X.H. Wang, C. Zhao, K.G. Qu, J.S. Ren, X.G. Qu, Label-free colorimetric detection of single nucleotide polymorphism by using single-walled carbon nanotube intrinsic peroxidase-like activity, Chem. Eur. J. 16 (2010) 3617–3621.
[25] J.Y. Chen, Y. Shu, H.L. Li, Q. Xu, X.Y. Hu, Nickel metal-organic framework 2D nanosheets with enhanced peroxidase nanozyme activity for colorimetric detection of H_2O_2, Talanta 189 (2018) 254–261.
[26] H.J. Zhang, X. Liang, L. Han, F. Li, "Non-naked" gold with glucose oxidase-like activity: a nanozyme for tandem catalysis, Small 14 (2018) 1803256.
[27] S. Luo, M.J. Li, V. Fung, B.G. Sumpter, J. Liu, Z.L. Wu, K. Page, New insights into the bulk and surface defect structures of ceria nanocrystals from neutron scattering study, Chem. Mat. 33 (2021) 3959–3970.
[28] F. Jonas, B. Lebeau, S. Siffert, L. Michelin, C. Poupin, R. Cousin, L. Josien, L. Vidal, M. Mallet, P. Gaudin, J.L. Blin, Nanoporous CeO2-ZrO2 oxides for oxidation of volatile organic compounds, ACS Appl. Nano Mater. 4 (2021) 1786–1797.
[29] X.W. Cheng, L. Huang, X.Y. Yang, A.A. Elzatahry, A. Alghamdi, Y.H. Deng, Rational design of a stable peroxidase mimic for colorimetric detection of H2O2 and glucose: A synergistic CeO_2/Zeolite Y nanocomposite, J. Colloid Interface Sci. 535 (2019) 425–435.
[30] Q.Y. Liu, Y.Y. Ding, Y.T. Yang, L.Y. Zhang, L.F. Sun, P.P. Chen, C. Gao, Enhanced peroxidase-like activity of porphyrin functionalized ceria nanorods for sensitive and selective colorimetric detection of glucose, Mater. Sci. Eng. C. Mater. Biol. Appl. 59 (2016) 445–453.
[31] V. Esposito, E. Traversa, Design of electroceramics for solid oxides fuel cell applications: playing with ceria, J. Am. Ceram. Soc. 91 (2008) 1037–1051.
[32] P. Jasinski, T. Suzuki, H.U. Anderson, Nanocrystalline undoped ceria oxygen sensor, Sens. Actuator B-Chem. 95 (2003) 73–77.
[33] A. Joseph, K.P.J. Mathew, S. Vandana, Zirconium-doped ceria nanoparticles as anticorrosion pigments in waterborne epoxy-polymer coatings, ACS Appl. Nano Mater. 4 (2021) 834–849.
[34] M.X. Luo, X.J. Qi, T.X. Ren, Y.X. Huang, A.A. Keller, H.T. Wang, B.R. Wu, H.P. Jin, F.T. Li, Heteroaggregation of CeO_2 and TiO_2 engineered nanoparticles in the aqueous phase: application of turbiscan stability index and fluorescence excitation-emission matrix (EEM) spectra, Colloid Surf. A-Physicochem. Eng. Asp. 533 (2017) 9–19.
[35] N. Thakur, P. Manna, J. Das, Synthesis and biomedical applications of nanoceria, a redox active nanoparticle, J. Nanobiotechnol. 17 (2019) 84.
[36] L.F. Sun, Y.Y. Ding, Y.L. Jiang, Q.Y. Liu, Montmorillonite-loaded ceria nanocomposites with superior peroxidase-like activity for rapid colorimetric detection of H_2O_2, Sens. Actuator B Chem. 239 (2017) 848–856.
[37] W.N. Yang, J. Li, J. Yang, Y. Liu, Z.P. Xu, X.F. Sun, F.D. Wang, D.H.L. Ng, Biomass-derived hierarchically porous CoFe-LDH/CeO_2 hybrid with peroxidase-like activity for colorimetric sensing of H_2O_2 and glucose, J. Alloy. Compd. 815 (2020), 152276.
[38] Y.Y. Huang, C.Q. Liu, F. Pu, Z. Liu, J.S. Ren, X.G. Qu, A. GO-Se, nanocomposite as an antioxidant nanozyme for cytoprotection, Chem. Commun. 53 (2017) 3082–3085.
[39] Z. Somosi, N.V. May, D. Sebok, I. Palinko, I. Szilagyi, Catalytic antioxidant nanocomposites based on sequential adsorption of redox active metal complexes and polyelectrolytes on nanoclay particles, Dalton Trans. 50 (2021) 2426–2435.
[40] N.B. Alsharif, G.F. Samu, S. Sáringer, S. Muráth, I. Szilagyi, A colloid approach to decorate latex particles with Prussian blue nanozymes, J. Mol. Liq. 309 (2020), 113066.
[41] N.B. Alsharif, K. Bere, S. Sáringer, G.F. Samu, D. Takács, V. Hornok, I. Szilagyi, Design of hybrid biocatalysts by controlled heteroaggregation of manganese oxide and sulfate latex particles to combat reactive oxygen species, J. Mat. Chem. B 9 (2021) 4929–4940.
[42] N.B. Alsharif, B. Katana, S. Murath, I. Szilagyi, Composite materials based on heteroaggregated particles: Fundamentals and applications, Adv. Colloid Interface Sci. 294 (2021), 102456.
[43] F. Caputo, M. Mameli, A. Sienkiewicz, S. Licoccia, F. Stellacci, L. Ghibelli, E. Traversa, A novel synthetic approach of cerium oxide nanoparticles with improved biomedical activity, Sci. Rep. 7 (2017) 4636.
[44] A.V. Delgado, E. Gonzalez-Caballero, R.J. Hunter, L.K. Koopal, J. Lyklema, Measurement and interpretation of electrokinetic phenomena - (IUPAC technical report), Pure Appl. Chem. 77 (2005) 1753–1805.
[45] H. Holthoff, S.U. Egelhaaf, M. Borkovec, P. Schurtenberger, H. Sticher, Coagulation rate measurements of colloidal particles by simultaneous static and dynamic light scattering, Langmuir 12 (1996) 5541–5549.
[46] G. Trefalt, I. Szilagyi, T. Oncsik, A. Sadeghpour, M. Borkovec, Probing colloidal particle aggregation by light scattering, Chimia 67 (2013) 772–776.
[47] M. Elimelech, J. Gregory, X. Jia, R.A. Williams, Particle deposition and aggregation: measurement, modeling, and simulation, Butterworth-Heinemann Ltd, Oxford, 1995.

[48] W. Brand-Williams, M.E. Cuvelier, C. Berset, Use of a free-radical method to evaluate antioxidant activity, Food Sci. Technol. -Lebensm. -Wiss. Technol. 28 (1995) 25–30.
[49] B. Jiang, D.M. Duan, L.Z. Gao, M.J. Zhou, K.L. Fan, Y. Tang, J.Q. Xi, Y.H. Bi, Z. Tong, G.F. Gao, N. Xie, A. Tango, G.H. Nie, M.M. Liang, X.Y. Yan, Standardized assays for determining the catalytic activity and kinetics of peroxidase-like nanozymes, Nat. Protoc. 13 (2018) 1506–1520.
[50] R. Bortamuly, G. Konwar, P.K. Boruah, M.R. Das, D. Mahanta, P. Saikia, CeO_2-PANI-HCl and CeO_2-PANI-PTSA composites: synthesis, characterization, and utilization as supercapacitor electrode materials, Ionics 26 (2020) 5747–5756.
[51] B.Y. Wang, B. Zhu, S.N. Yun, W. Zhang, C. Xia, M. Afza, Y.X. Cai, Y.Y. Liu, Y. Wang, H. Wang, Fast ionic conduction in semiconductor CeO_2-delta electrolyte fuel cells, NPG Asia Mater. 11 (2019) 51.
[52] X.B. Liu, F.M. Meng, B. Yu, H. Wu, Self-assembly synthesis of flower-like CeO_2/MoS_2 heterojunction with enhancement of visible light photocatalytic activity for methyl orange, J. Mater. Sci. Mater. Electron. 31 (2020) 6690–6697.
[53] C.T. Nottbohm, C. Hess, Investigation of ceria by combined Raman, UV–vis and X-ray photoelectron spectroscopy, Catal. Commun. 22 (2012) 39–42.
[54] L. Ovari, S.K. Calderon, Y. Lykhach, J. Libuda, A. Erdohelyi, C. Papp, J. Kiss, H. P. Steinruck, Near ambient pressure XPS investigation of the interaction of ethanol with Co/CeO_2(111), J. Catal. 307 (2013) 132–139.
[55] E.K. Goharshadi, S. Samiee, P. Nancarrow, Fabrication of cerium oxide nanoparticles: characterization and optical properties, J. Colloid Interface Sci. 356 (2011) 473–480.
[56] J.E. Spanier, R.D. Robinson, F. Zheng, S.W. Chan, I.P. Herman, Size-dependent properties of CeO_2-y nanoparticles as studied by Raman scattering, Phys. Rev. B 64 (2001), 245407.
[57] M. Runowski, N. Stopikowska, S. Lis, UV-Vis-NIR absorption spectra of lanthanide oxides and fluorides, Dalton Trans. 49 (2020) 2129–2137.
[58] P.F. Ji, J.L. Zhang, F. Chen, M. Anpo, Ordered mesoporous CeO_2 synthesized by nanocasting from cubic Ia3d mesoporous MCM-48 silica: Formation, characterization and photocatalytic activity, J. Phys. Chem. C. 112 (2008) 17809–17813.
[59] K. Bohinc, K. Korade, K. Jerin, N. Lesic, M. Dakovic, G. Drazic, J.F. Dufreche, D. Kovacevic, Experimental and theoretical study of morphological and charging properties of truncated octahedron and cubic ceria nanoparticles: Implications for biomedical applications, ACS Appl. Nano Mater. 4 (2021) 1434–1444.
[60] S. Muráth, S. Sáringer, Z. Somosi, I. Szilagyi, Effect of ionic compounds of different valences on the stability of titanium oxide colloids, Colloid Inter. 2 (2018) 32.
[61] M. Pavlovic, P. Rouster, E. Bourgeat-Lami, V. Prevot, I. Szilagyi, Design of latex-layered double hydroxide composites by tuning the aggregation in suspensions, Soft Matter 13 (2017) 842–851.
[62] D. Bauer, H. Buchhammer, A. Fuchs, W. Jaeger, E. Killmann, K. Lunkwitz, R. Rehmet, S. Schwarz, Stability of colloidal silica, sikron and polystyrene latex influenced by the adsorption of polycations of different charge density, Colloid Surf. A 156 (1999) 291–305.
[63] C. Vasti, A. Borgiallo, C.E. Giacomelli, R. Rojas, Layered double hydroxide nanoparticles customization by polyelectrolyte adsorption: mechanism and effect on particle aggregation, Colloid Surf. A 533 (2017) 316–322.
[64] K.R. Ratinac, O.C. Standard, P.J. Bryant, Lignosulfonate adsorption on and stabilization of lead zirconate titanate in aqueous suspension, J. Colloid Interface Sci. 273 (2004) 442–454.
[65] A. Tiraferri, M. Borkovec, Probing effects of polymer adsorption in colloidal particle suspensions by light scattering as relevant for the aquatic environment: an overview, Sci. Total Environ. 535 (2015) 131–140.
[66] T.E. Bridges, M.P. Houlne, J.M. Harris, Spatially resolved analysis of small particles by confocal Raman microscopy: Depth profiling and optical trapping, Anal. Chem. 76 (2004) 576–584.
[67] S.H. Park, S. Wei, B. Mizaikoff, A.E. Taylor, C. Favero, C.H. Huang, Degradation of amine-based water treatment polymers during chloramination as N-nitrosodimethylamine (NDMA) precursors, Environ. Sci. Technol. 43 (2009) 1360–1366.
[68] M. Li, H.Y. Su, Y. Tu, Y.Z. Shang, Y. Liu, C.J. Peng, H.L. Liu, Development and application of an efficient medium for chromogenic catalysis of tetramethylbenzidine with horseradish peroxidase, ACS Omega 4 (2019) 5459–5470.
[69] L. Rastogi, D. Karunasagar, R.B. Sashidhar, A. Giri, Peroxidase-like activity of gum kondagogu reduced/stabilized palladium nanoparticles and its analytical application for colorimetric detection of glucose in biological samples, Sens. Actuator B-Chem. 240 (2017) 1182–1188.
[70] X.N. Hu, A. Saran, S. Hou, T. Wen, Y.L. Ji, W.Q. Liu, H. Zhang, X.C. Wu, Rod-shaped Au@PtCu nanostructures with enhanced peroxidase-like activity and their ELISA application, Chin. Sci. Bull. 59 (2014) 2588–2596.